Research Article | Vol. 28, No. 21 / 12 October 2020 / Optics Express 30432
Optics EXPRESS

Phase sensitive low-coherence interferometry using microwave photonics

JUAN CLEMENT, HAROLDO MAESTRE, GERMÁN TORREGROSA, AND CARLOS R. FERNÁNDEZ-POUSA*

Engineering Research Center (I3E), Dep. of Communications Engineering, Universidad Miguel Hernández, 03202 Elche, Spain
c.pousa@umh.es

Abstract: We report on a low-coherence interferometer based on Microwave Photonics (MWP) which allows, for the first time to the best of our knowledge, stable determination of the interferogram's phase. The interferometer is built on suppressed carrier, double-sideband modulation, dispersive propagation in a chirped fiber Bragg grating, demodulation by electro-optical frequency down-conversion, and suitable signal processing techniques to account for modulation impairments. Taking as a reference a direct normalization of the link's microwave response, the system retrieves high-resolution interferograms, both in amplitude and phase and free from distortion induced by higher-order dispersion, in an optical path difference of 16.3 mm, surpassing previously reported values based on MWP implementations. We present representative applications targeted to the characterization of C-band sources and components, such as direct analysis of interferograms with 5.5 fs temporal resolution, Fourier-transform spectroscopy with 14 GHz spectral resolution, and optical low-coherence reflectrometry of the impulse response's amplitude of fiber Bragg gratings with 0.55 μm spatial resolution.

1. Introduction

Fiber systems based on low-coherence interferometry (LCI) have been used over the years for the high-resolution characterization of sources, components, and sensors [1]. Fourier-transform (FT) spectrometers take advantage of the Fourier duality between the interferogram and the optical spectrum for the analysis of sources [2,3] and wavelength encoded sensors [4], and Optical Low-Coherence Reflectometers (OLCR) [5–9], Optical Coherence Tomography (OCT) systems [10,11] and displacement sensors [12] locate reflective events by use of the sharp interference of low-coherence light. A major endeavor in these systems is to accurately record the interferogram's phase, since this allows to determine the spectrum of an optical wave or the vector information of the device or system under consideration. For this purpose, phase sensitive LCI systems conventionally use an auxiliary laser to monitor the optical path difference (OPD) scan [2,3,8,9,13–15].

As a basic interference phenomenon, LCI continues to attract attention in different contexts, and also in Microwave Photonics (MWP), where there has recently been an increasing interest in optical metrology systems for optical fiber sensors [16,17]. In this regard, MWP offers opportunities for the analysis of optical waves through the use of wideband radio-frequency (RF) modulation, custom definition of optical circuits using standard splitting, filtering and propagation technologies, high stability of the RF interference, and ease of reconfigurability by purely electronic means. Within this context, the use of a well known MWP architecture, namely an analog-modulated dispersive link fed with a broadband source (BBS) [18], has been identified as a simple means to characterize fiber Bragg grating (FBG) sensors [19–22], interferometers [23,24] or multilayered samples [25]. In [26] we demonstrated the equivalence of this architecture with a self-referenced double-interferometer LCI system [12,27], where a first, static interferometer is used to probe the device under test (DUT), and the second interferometer,

#403176 https://doi.org/10.1364/OE.403176
Journal © 2020 Received 22 Jul 2020; revised 13 Sep 2020; accepted 14 Sep 2020; published 28 Sep 2020

Optics EXPRESS

built on MWP concepts, is used to scan the OPD through standard electrical vector network analysis (VNA). The approach is attractive since high-resolution OPD scans are performed without the need of mechanical parts, the double interferometer allows for absolute distance measurements and, as an additional benefit, the relationship between path delays and scanning RF tones can be adjusted through the value of dispersion. Also, and due to the high accuracy of the electronic oscillators' frequency, the corresponding accuracy in path delays is in practice only limited by the stability of the imparted dispersion. We also identified, however, a number of shortcomings limiting LCI range and resolution: the broadening, distortion, and fading of the RF resonance representing the LCI peak was due to the link's higher-order dispersion (HOD) and to the carrier suppression effect (CSE) inherited from the amplitude modulation format used. Subsequent efforts have been targeted to overcome these issues with single-sideband modulation [28], alternative MWP architectures [29], a double pass in the interferometer [30], and also to provide increases in scanning speed [31] and sensitivity [32]. In all these implementations, the analysis is focused in the interferogram's amplitude, typically locating the position of test reflectors by use of the RF resonance, and little attention seems to have been paid to the stability of the interferogram's phase extracted by this procedure.

In this paper we present, for the first time to the best of our knowledge, a phase sensitive MWP LCI system based on double-sideband with suppressed carrier (DSB-SC) modulation, dispersive propagation in a chirped FBG (CFBG), and demodulation by electro-optical frequency down-conversion, thus benefiting from the common-path propagation of the modulated and dispersed waves responsible of the optical interference. Using only 20 GHz of RF bandwidth and a direct normalization of the link's amplitude and phase response, our system retrieves the amplitude and phase of interferograms in an OPD range of 16.3 mm, outperforming previously reported values based on related MWP approaches. This range allows to explore a number of LCI applications targeted to sources and components in the C band, such as a direct analysis of interferograms, FT spectroscopy, and OLCR characterization of FBG. Built from a combination of frequency up- and down-conversion, the system, when operated with monochromatic light, can be understood as a Frequency-Shifted Interferometer (FSI) [33–35]. As will be shown below, however, it is the inclusion of a dispersive element together with broadband illumination what provides the possibility to record low-coherence interferograms.

These results have been attained by a number of improvements with respect to our initial demonstration [26]. DSB-SC modulation shows no CSE and provides a twofold increase in range for given dispersion and modulation bandwidth. The broadband CFBG is a non-standard device providing stable 10-km dispersion compensation in the C band with negligible HOD [36]. This element has previously been used to demonstrate FT spectroscopy using conventional amplitude modulation [37]. Additionally, the use of a second electro-optical modulator to perform homodyne down-conversion avoids the use of a harmonic VNA (i.e., a VNA whose receiver is tuned to a harmonic of the stimulus frequency). The low bandwidth detection enables the cost-effective use of high-sensitive detectors and high-depth digitizers. Finally, impairments due to modulators' harmonic distortion and bias drifts have been numerically compensated for by suitable signal processing techniques.

This paper is organized as follows. In Section 2 we analyze the MWP architecture, the normalization procedure leading to the interferogram, and the signal processing techniques used. Section 3 introduces the experimental setup and the normalization traces. In Section 4 we present the characterization of several C-band sources and reflectors and the determination of performance parameters in FT spectroscopy. Finally, we end in Section 5 with our conclusions.

2. Principle of operation

Referring to Fig. 1, the system can be presented as follows. A polarized laser line from a tunable laser source (TLS) with optical frequency ω_0, electric field $\mathcal{E}_0(t) = E_0 \exp(j\omega_0 t)$ and power

Optics EXPRESS

$P_0 = |E_0|^2$ is injected in a first push-pull electro-optic Mach-Zehnder modulator (MZM1). The modulator is biased at minimum transmission and driven by a RF tone at frequency Ω, so that the output optical field is given by:

$$\begin{aligned}\mathcal{E}_1(t) &= a_1(\Omega)\cos[\Omega t + \varphi_1(\Omega)]\mathcal{E}_0(t) \\ &= \frac{E_0}{2}a_1(\Omega)e^{j(\omega_0+\Omega)t+j\varphi_1(\Omega)} + \frac{E_0}{2}a_1(\Omega)e^{j(\omega_0-\Omega)t-j\varphi_1(\Omega)}\end{aligned} \tag{1}$$

with $a_1(\Omega)$ and $\varphi_1(\Omega)$ the amplitude and phase responses, respectively, of the concatenation of modulator, RF cables and splitter, and where we have temporarily neglected harmonic distortion. The amplitude response is related to the modulation voltage amplitude V_{rf} as $a_1(\Omega) = 2J_1(\pi V_{\mathrm{rf}}/V_\pi(\Omega))$, with $V_\pi(\Omega)$ the modulator's half-wave voltage and J_1 the Bessel function of the first kind and order one.

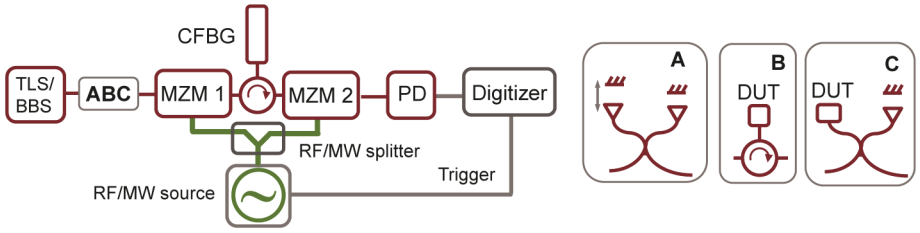

Fig. 1. Schematics of the system. The box (ABC) refers to different measurement configurations, shown in detail on the right and not used in the normalization procedure.

The modulated optical wave $\mathcal{E}_1(t)$ shows two optical sidebands at frequencies $\omega_0 \pm \Omega$. The CFBG acts as a dispersive delay line (DDL) imparting on these sidebands propagation phases $\phi(\omega_0 \pm \Omega) = \phi(\omega_0) \mp \Omega\tau_0$, with τ_0 the group delay at frequency ω_0. The dispersed wave $\mathcal{E}_1'(t)$ is subsequently remodulated by a second modulator (MZM2), synchronously driven at the same tone Ω to produce a second DSB-SC modulation $\mathcal{E}_2(t) = a_2(\Omega)\cos[\Omega t + \varphi_2(\Omega)]\mathcal{E}_1'(t)$. The resulting wave is given by:

$$\begin{aligned}\mathcal{E}_2(t) = \frac{1}{4}a_1(\Omega)a_2(\Omega)E_0e^{j\omega_0 t+j\phi(\omega_0)} \times \big[&2\cos\left(\Omega\tau_0 - \varphi_1(\Omega) + \varphi_2(\Omega)\right) \\ &+ e^{j2\Omega(t-\tau_0/2)+j\varphi_1(\Omega)+j\varphi_2(\Omega)} + e^{-j2\Omega(t-\tau_0/2)-j\varphi_1(\Omega)-j\varphi_2(\Omega)}\big]\end{aligned} \tag{2}$$

and shows a carrier component, where we observe the interference induced by frequency up and down-conversion, together with two sidebands, now at optical frequencies $\omega_0 \pm 2\Omega$.

Hence, if the photodiode's (PD) bandwidth is lower than 2Ω, the voltage $\mathcal{V}_0(\Omega)$ recorded by the digitizer is proportional to the average power of $\mathcal{E}_2(t)$, which is simply the sum of the power at the carrier and those of the two sidebands. According to Eq. (2), the optical power at the carrier wavelength is $\frac{1}{8}TA(\Omega)P_0[1 + \cos(2\Omega\tau_0 - \varphi(\Omega))]$, with $A(\Omega) = a_1^2(\Omega)a_2^2(\Omega)$ the product of modulators' power transfer functions, $\varphi(\Omega) = 2[\varphi_1(\Omega) - \varphi_2(\Omega)]$ the double of their difference in phase response, and T the system's insertion loss when P_0 is referred to the input of the first modulator. Also, each of the sidebands at $\omega_0 \pm 2\Omega$ provides an additional power $\frac{1}{16}TA(\Omega)P_0$. The recorded voltage is thus:

$$\mathcal{V}_0(\Omega) = \frac{1}{4}Z_L\mathcal{R}TP_0A(\Omega) + \frac{1}{8}Z_L\mathcal{R}TP_0A(\Omega)\cos[2\Omega\tau_0 - \varphi(\Omega)] \tag{3}$$

with $\mathcal{R}$ the photodiode's responsivity and Z_L the load's impedance. As a function of Ω, voltage $\mathcal{V}_0(\Omega)$ comprises of baseband and bandpass components, this last centered at a period in frequency of $1/(2\tau_0)$ and representing the interference of the two optical sidebands, which are brought back

Optics EXPRESS

to the original optical frequency ω_0 by the second modulator in a common path configuration. Note that the factor of 8 in the denominator of the second term accounts for an intrinsic 9 dB power penalty associated to the processes of modulation and down-conversion. Equation (3) describes a form of FSI, a technique that has been widely employed to retrieve the location (τ_0) and reflectivity of events by inverse Fourier transforming the interferogram [33–35].

In Fig. 2 we illustrate Eq. (2) using the experimental system described in the following section. In this plot we show the optical spectrum, measured at the output of the second modulator, of a 1550 nm carrier modulated around $\Omega/(2\pi) \simeq 10$ GHz when this frequency is fine tuned to reach the interference's maximum (blue trace) and minimum (orange trace) at the carrier wavelength. At the minimum, the power decreases to a value determined by the attenuation and the suppression of the carrier in the two modulators biased at minimum transmission. This value can be determined by switching off the modulation, as is shown with a yellow trace. The measured total extinction ratio, relative to the carrier power measured before the first modulator, is −67.6 dB, including an insertion loss T of 10 dB. Also observable are residual sidebands at ±10 GHz, generated by the first modulator and suppressed only by the second. The relative carrier power at the interference's maximum, $\frac{1}{4}TA(\Omega)$, is −36.3 dB, as so the modulation and down-conversion loss factor $A(\Omega)$ is −20.3 dB at 10 GHz.

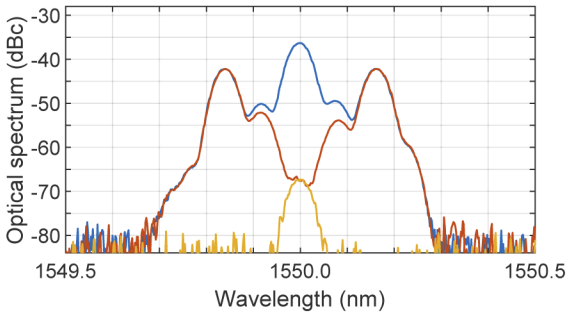

Fig. 2. Optical spectrum of the modulated, dispersed and down-converted waves at $\Omega/(2\pi) \sim 10$ GHz over a 1550 nm carrier under constructive (blue) and destructive (orange) interference. Yellow: power spectrum when the modulation is off. The spectrum is referred to the carrier power P_0 measured at the input of the first modulator.

Voltage $\mathcal{V}_0(\Omega)$ suffers from a background component due to the modulators' finite extinction ratio, and also from variations due to their bias drifts, which were not controlled in our experiments. After typically half an hour of warm-up time, these effects are sufficiently slow to allow for stable measurements in time spans of the order of minutes. Inclusion of modulators' harmonic distortion in the analysis results in the appearance of spurious tones in $\mathcal{V}_0(\Omega)$ of the form $\cos[n\Omega\tau_0 - n\varphi(\Omega)/2]$ with $n \neq 2$. These terms are bandpass signals centered at a period in frequency $1/(n\tau_0)$, and can be removed by Fourier transforming $\mathcal{V}_0(\Omega)$ to a new signal $v_0(t)$ since they are concentrated at $t = n\tau_0$. The second term in (3) representing the interferogram can be isolated by filtering $v_0(t)$ around $t = 2\tau_0$.

When the system is fed with a BBS, described by an electric field $\mathcal{E}(t)$ and an optical spectral density $S(\omega)$, each of its spectral components undergoes the same transformation as that written in Eq. (3), yielding a voltage:

$$\mathcal{V}(\Omega) = \frac{1}{8} Z_L \mathcal{R} T A(\Omega) \int_0^\infty d\omega S(\omega) \cos[2\Omega\tau(\omega) - \varphi(\Omega)] \tag{4}$$

Here we have omitted the baseband component and assumed that $A(\Omega)$ and $\varphi(\Omega)$ are independent of wavelength. Each modulated wavelength experiences a different group delay $\tau(\omega)$. Assuming

Optics EXPRESS

purely first order dispersion we may write $\tau(\omega) = \tau_0 + \tau_0'(\omega - \omega_0)$, with $\tau_0' = d\tau/d\omega$ the dispersion coefficient and τ_0 the group delay at a reference frequency ω_0. Using this formula in Eq. (4) we observe that $\mathcal{V}(\Omega)$ is again a bandpass function with spectral content centered at frequency $1/(2\tau_0)$, so that it can be Hilbert transformed to an analytic signal $\mathcal{V}^c(\Omega)$ given by:

$$\begin{aligned}\mathcal{V}^c(\Omega) &= \frac{1}{8} Z_L \mathcal{R} T A(\Omega) e^{-j\varphi(\Omega)} \int_0^\infty d\omega S(\omega) e^{j2\Omega\tau_0 + j2\Omega\tau_0'(\omega-\omega_0)} \\ &= \frac{1}{8} Z_L \mathcal{R} T A(\Omega) e^{-j\varphi(\Omega)} \Gamma(2\Omega\tau_0') e^{j2\Omega\tau_0}\end{aligned} \tag{5}$$

where $\Gamma(u) = \langle \mathcal{E}(t)^* \mathcal{E}(t+u) \rangle e^{-j\omega_0 u} = \int d\omega\, S(\omega) e^{j(\omega-\omega_0)u}$ is the field's autocorrelation with its phase shifted to that of the reference frequency ω_0, the asterisk stands for complex conjugation, and we have denoted the field's statistical average with angle brackets. Finally, to subtract from $\mathcal{V}^c(\Omega)$ the frequency response of the driving electronics, Eq. (5) is divided by function

$$\mathcal{V}_0^c(\Omega) = \frac{1}{8} Z_L \mathcal{R} T P_0 A(\Omega) e^{-j\varphi(\Omega) + j2\Omega\tau_0} \tag{6}$$

describing the detected voltage when the system is fed with a laser line at frequency ω_0. This procedure also removes from Eq. (5) the last oscillatory term and therefore its dependence on the reference delay τ_0. The result is the sought-for interferogram in complex form,

$$\frac{\mathcal{V}^c(\Omega)}{\mathcal{V}_0^c(\Omega)} = \frac{1}{P_0} \Gamma(u = 2\Omega\tau_0') \tag{7}$$

where the time lag u is controlled by tone Ω and scaled by the dispersion coefficient τ_0'. Note that, once τ_0' is determined, any given value of Ω provides an absolute reference for the time lag u, and that this time lag can be scanned using different ranges of modulation tones. Also note that, given available values of bandwidth $\Omega_{\max}$ and dispersion τ_0', the use of DSB-SC modulation provides a temporal range $u_{\max} = 2\Omega_{\max}\tau_0'$ which doubles that of previous demonstrations using the conventional AM modulation with the modulators biased in quadrature or other, alternative modulation formats [28–30].

The raw temporal step, δu, or one-point resolution of our low-coherence interferograms, depends on the frequency step $\Delta\Omega$ used to sequentially scan the temporal range, and is given by $\delta u = 2\Delta\Omega\tau_0'$. In LCI systems, ranges are expressed as OPD, or single-pass distance in free space (OPD = cu, with c the speed of light in vacuum). The LCI (two-point) spatial resolution equals the source's coherence length ℓ_c, which is the FWHM of the amplitude peak that reflects the low-coherence interference. The coherence length is inversely proportional to the source's spectral width $\Delta\nu$, with a proportionality constant that depends on the form of the spectrum. In our LCI experiments, we use a BBS which has a roughly square-like spectrum. For a perfect square spectrum, the autocorrelation $\Gamma(u)$ is sinc-like and results in a relationship $\ell_c = 1.21c/\Delta\nu$. In OLCR systems, the scan is conventionally expressed in terms of double pass distance, $z = cu/(2n_g)$ with n_g the fiber's group refractive index. The standard two-point OLCR resolution in fiber is thus given by $\delta z_2 = \ell_c/(2n_g)$ [1]. As will be shown below, however, in our OLCR characterization of the impulse response of FBGs the relevant resolution is the one-point spatial resolution, given by $\delta z = c\delta u/(2n_g)$. Finally, in FT spectroscopy, the inteferograms are extended in complex form to negative delays using the hermiticity condition $\Gamma(-u) = \Gamma(u)^*$. The spectral resolution $\delta\nu$ is given by $\delta\nu = 1.21\kappa/(2u_{\max})$, where κ>1 describes the increase in $\delta\nu$ when a window is applied to $\Gamma(u)$ before the FT and $\kappa = 1$ in the absence of windowing. The wavelength range in FT spectroscopy, however, is here limited by the reflection band of the CFBG grating used to implement the DDL.

It is apparent from the previous discussion that the ability to record the complex interferogram requires that the involved dispersive delays are stable during the normalization and measurement

Optics EXPRESS

procedures. The implementation of the DDL with a fiber coil may fail in meeting this requirement due to thermal variations and mechanical stress in the fiber. The same shortcoming occurs, for instance, in the distribution of RF tones through fiber lines [38]. Other, more costly, alternatives include the use of programmable optical phase filters [39]. In our setup, the DDL used was a low-ripple, athermally-packaged, C-band CFBG, described in the following section. We finally stress that the recovery of the BBS autocorrelation $\Gamma(u)$ relies on the fact that the dispersive element shows negligible HOD τ_0''. Conventional CFBG for dispersion compensation of standard single-mode fiber (SMF) would distort the interferograms and, although they can be numerically corrected [40,41], this has not been necessary here.

3. Experimental setup and normalization

In our implementation, and referring again to Fig. 1, two push-pull Mach-Zehnder electro-optic modulators of bandwidth 20 GHz (JDSU AM150 and Avanex SD20) were used to implement the DSB-SC modulation and down-conversion stages, both at an input RF power of +16 dBm and without active bias control. The CFBG (Proximion) was a broadband device (1540-1560 nm) with a dispersion at 1550 nm of −170.04 ps/nm ($\tau_0' = 216.87$ ps^2/rad), negligible HOD ($\tau_0'' = -0.05$ ps^3/rad^2) and low ripple (rms phase ripple <0.02 rad). Additional details can be consulted in [36]. As mentioned before, the system's insertion loss T measured from the first modulator was 10 dB and includes a non-uniform CFBG loss of 1.8 ± 0.2 dB. The modulators were driven by a RF or a microwave (MW) signal generator, to be described below. The detector was a standard 1-GHz pin photodiode (Thorlabs DET01CFC, $\mathcal{R} = 0.95$ A/W) whose bandwidth was limited to a few tens of kHz by the 1-MΩ load imposed by a 14-bit digitizer (Digilent Analog Discovery 2) operated at a sampling rate of 100 kHz.

In a first test we fed the system with a monochromatic laser line at 1550 nm extracted form our TLS (Keysight N7711A) and programmed a narrowband RF sweep from $\Omega/(2\pi) = 10$ GHz to 10.05 GHz in steps of 25 kHz to exemplify a few cycles of the interference pattern given by Eq. (3). The result is plotted in Fig. 3. In the first plot, Fig. 3(a), the frequency sweep shown in blue and starting at 0.6 s is governed by the MW source (Anritsu MG3690C). The frequency period between interference's maxima is $1/(2\tau_0) = 9.25$ MHz, and is due to a delay τ_0 in a SMF length between modulators of 10.8 m. The equivalent OPD step is as low as 4 nm. This experiment also permits to visualize the interferometer's short-term stability: the constant voltage level at 10 GHz shown in orange has a standard deviation of 0.59 mV. In terms of the inteferometer's phase, $\Phi(\Omega) = 2\Omega\tau_0 - \varphi(\Omega)$, this corresponds to a phase deviation of 0.14 deg or to a deviation in OPD of 0.6 nm. The yellow trace is the reading when the laser is switched off and represents the system's noise floor, with a standard deviation of 0.18 mV. The excess in standard deviation of the 10-GHz interference level is attributed to thermal effects within the light path between modulators. Figure 3(b) is a zoom view showing the structure of the frequency steps and the stability of the 10-GHz level.

The system was then completed to the LCI setup, as described in Eqs. (5)–(7). The BBS was a polarized ASE source with a roughly flat spectral density in the CFBG reflection band. The available RF bandwidth was scanned from 2 MHz up to $\Omega_{\max}/(2\pi)$ =20 GHz to display a total temporal range $u_{\max} = 2\Omega_{\max}\tau_0' = 54.5$ ps. This corresponds to an OPD of 16.3 mm in free space or 10.9 mm in fiber, ranges that are halved in reflectometric measurements. The frequency step was $\Delta\Omega/(2\pi)$ =2 MHz, and had a duration of ~3 ms. Since the lowest frequency delivered by the MW signal generator is 10 MHz, it was necessary to use a second RF source (TTi TG4001) whose scanning range was partially coincident with the MW signal generator, from 2 MHz to 30 MHz, including an additional tone at 75 kHz to help interpolate $\mathcal{V}(\Omega)$ for $\Omega \to 0$. The temporal step of our interferograms is thus $\delta u = 2\Delta\Omega\tau_0' = 5.45$ fs (1.63 μm in free space, single pass). It was limited by the number of frequency steps that can be sequentially delivered by our MW generator (10^4) which were chosen to evenly sweep the total available

Optics EXPRESS

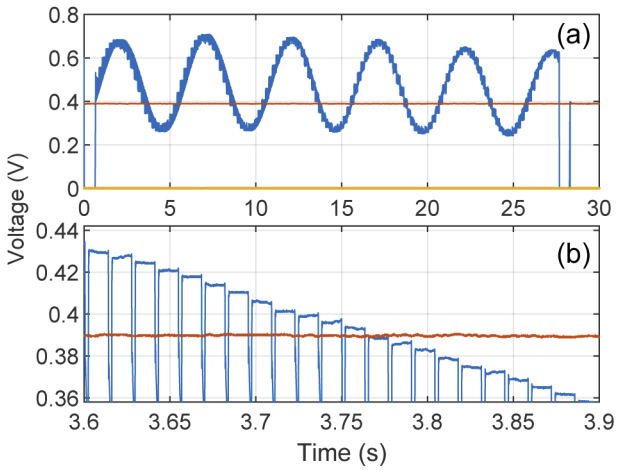

Fig. 3. (a) Blue: digitized voltage $\mathcal{V}_0(\Omega)$ corresponding to a laser line at 1550 nm with $P_0 = 3.5$ dBm. The initial value of the RF is $\Omega/(2\pi) = 10$ GHz, increasing in 25 kHz steps of duration ~10 ms up to 10.05 GHz. Orange: constant RF level at 10 GHz. Yellow: noise floor when the laser is switched off. (b) Zoom of the blue and orange traces in (a) showing the structure of the 25-kHz RF steps. The glitches are due to the commutation of the MW source.

temporal range. For each frequency Ω, the constant output of the digitizer was averaged over the step duration by first detecting the commutation glitches, which were gated by a synchronization signal from the RF/MW source, and then averaging the level over the interval between glitches. The $\Omega \to 0$ value of signal $\mathcal{V}(\Omega)$ was then interpolated and, after Hilbert transform, it was divided in complex form by a 1550-nm normalization trace $\mathcal{V}_0^c(\Omega)$ taken using the same range and frequency steps. This normalization was previously filtered around frequency $1/(2\tau_0)$. The scan time was about 3 seconds per mm of OPD.

Figure 4 shows the plot of the amplitude $|\mathcal{V}_0^c(\Omega)|/(Z_L\mathcal{R}P_0)$ and phase $\varphi(\Omega)$ of a normalization trace at $P_0 = -5$ dBm, in this last case after the subtraction of the linear phase term describing the propagation delay τ_0 between modulators. According to Eq. (6), the amplitude equals $\frac{1}{8}TA(\Omega)$ and represents the effective optical loss experienced by a given input power. It shows a peak value of −30.6 dB at 230 MHz followed by a roll-off due to the bandwidth limitations of modulators, cables and RF splitter, which results in a decrease in signal-to-noise ratio for increasing delays in all our interferograms. It the middle of this roll-off, the curve reproduces the value −39.3 dB at 10 GHz inferred from our analysis of Fig. 2. Below 230 MHz, the amplitude is limited by the modulators' response, whereas the ripples observed in the phase are likely due to small impedance mismatches within the RF path. We also compared six of these normalization traces taken in a span of four weeks in standard laboratory conditions. The manual polarization alignment before modulators (not shown in Fig. 1) and bias drifts result in global variations in the amplitude response of ~1 dB. Once normalized to its maximum value, the remaining rms amplitude variation, averaged over the whole bandwidth, was <0.2 dB for all the analyzed traces. The global delay τ_0 showed a maximum variation among traces of $\Delta\tau_0 = 7$ ps. According to Eq. (5), this variation translates into a variation in the interferogram's frequency of $\Delta\omega = \Delta\tau_0/\tau_0'$, with value 7 GHz (56 pm in the C band), a figure that represents an estimate of the accuracy in the determination of optical frequencies due to environmental changes. The remaining phase variation after subtraction of the linear phase, in turn, was lower than 2 deg rms.

Optics EXPRESS

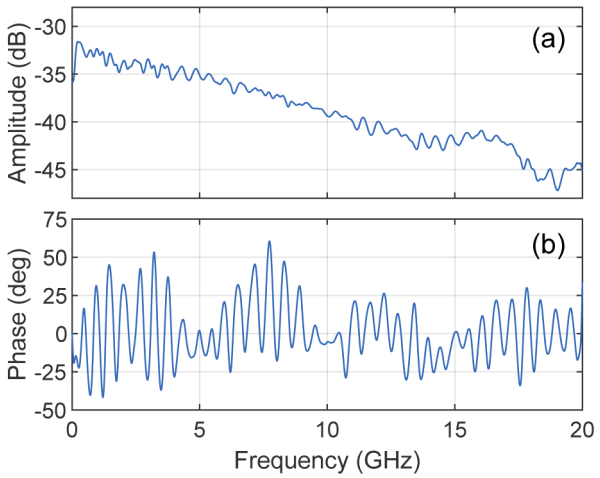

Fig. 4. (a) Amplitude $10\log_{10}[|\mathcal{V}_0^c(\Omega)|/(Z_L\mathcal{R}P_0)]$ and (b) phase $\varphi(\Omega)$ of a normalization trace.

4. Results

Our first experiment was targeted to confirm the system's OPD range. The BBS was followed by a Michelson interferometer placed before the first modulator and built from a 3 dB splitter, fiber collimators, and dielectric mirrors, as shown by scheme A in Fig. 1. The interferogram's amplitude, depicted in Fig. 5, showed different peaks with a uniform FWHM $\delta\ell$ of 142 ± 3 μm as one of the mirrors was displaced in steps of 1 mm, confirming the expected OPD range and the absence of peak broadening and fading due to CSE or HOD. The small distortion in the peaks' structure, visible as an asymmetry in its low-power sidelobes, is ascribed to the CFBG's residual HOD.

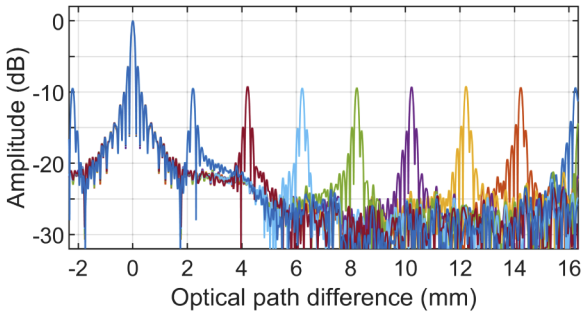

Fig. 5. Amplitude $10\log_{10}|\Gamma(u)|$ of the complex low-coherence interferogram describing the incidence of a BBS in an interferometer for different path imbalances, increasing from 2.2 mm in 2-mm steps.

We then analyzed the typical BBS used in our experiments, directing the broadband light to the first modulator, retrieving its autocorrelation $\Gamma_{\mathrm{BBS}}(u)$, and computing the FT spectrum. We also measured the optical spectrum using a standard dispersive grating-based OSA (Agilent 86142B, 60 pm resolution). The measurement was taken from the detector's side so that both spectra suffer from the same non-uniform CFBG loss and are therefore comparable. We finally computed the inverse Fourier transform (IFT) of the OSA spectrum to compare it with the experimental interferogram. The resolution of this IFT was increased by zero padding the

Optics EXPRESS

spectrum, a procedure which is enabled here since the BBS spectra is bandlimited due to its pass through the CFBG.

The optical spectrum, together with the amplitude and phase of the interferogram, are presented in Fig. 6; in orange those corresponding to the OSA spectrum and its IFT, and in blue the interferogram's amplitude and phase together with its FT spectrum. The agreement of both approaches is excellent. The optical spectrum in Fig. 6(a) is square like and contained in the ~20-nm CFBG reflection bandwidth. The interferogram's amplitude, shown in Fig. 6(b), presents a coherence length ℓ_c of 144 μm, in agreement with Fig. 5 and also with the expected value of a square optical spectrum with width $\Delta\nu = 2.5$ THz. The interferogram's amplitude indeed shows, for low values of the OPD, the typical sinc functional form. As for the phase in Fig. 6(c), the expected behaviour of $\arg\Gamma_{\mathrm{BBS}}(u)$ for low values of time lag u or OPD is proportional to the BBS's central frequency $\overline{\omega} = \int \omega S(\omega)d\omega/P_0$, with $S(\omega)$ the optical spectral density and $P_0 = \int S(\omega)d\omega$ the total BBS power. This can be deduced by expanding the exponential term in the IFT to first order:

$$\Gamma_{\mathrm{BBS}}(u) = \int_{\omega_l}^{\omega_h} S(\omega)e^{j\omega u}d\omega \simeq \int_{\omega_l}^{\omega_h} S(\omega)(1+j\omega u)d\omega = P_0\,(1+j\overline{\omega}u) \simeq P_0 e^{j\overline{\omega}\,u} \tag{8}$$

Here, ω_l (resp. ω_h) is the optical frequency corresponding to the spectrum's edge with longer (resp. shorter) wavelength. The plot in Fig. 6(c) has been referred to this central frequency, which corresponds to a wavelength of 1549.79 nm. The depicted phase is thus zero for low values of the OPD, and is followed by approximated π phase jumps at the amplitude's notches, resembling the expected behaviour of the ideal sinc autocorrelation of a perfect square spectrum.

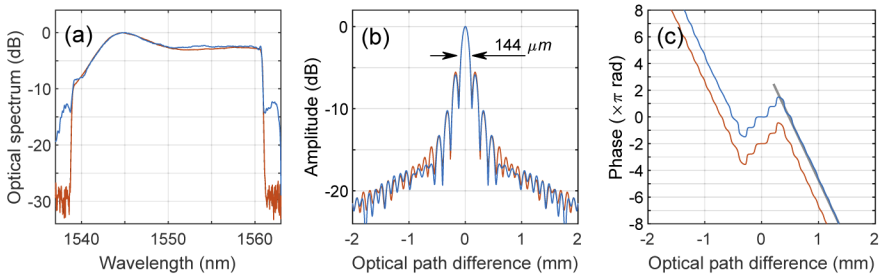

Fig. 6. (a) FT (blue) and OSA (orange) spectra of the BBS. (b) Interferogram's amplitude (blue), and amplitude of the OSA spectrum's IFT (orange). (c) Interferogram's phase (blue), and phase of the OSA spectrum's IFT (orange, shifted by -2π), both referred to the BBS's central frequency. Gray line: linear fit of the asymptotic phase.

After an OPD of 380 μm, and therefore well above the coherence length, the phase shows a linear decreasing trend that describes a behaviour of the autocorrelation of the form $\Gamma_{\mathrm{BBS}}(u) \propto \exp(j\omega_l u)$, with ω_l corresponding to the wavelength 1560.82 nm of the steepest edge of the BBS spectrum. The linear fit to this decreasing phase has been depicted with a gray line in Fig. 6(c). This change in the phase behaviour is a consequence of the asymptotic limit for large $|u|$ of the IFT that defines $\Gamma_{\mathrm{BBS}}(u)$ in terms of the spectrum [42], which is determined by the different spectral density at the spectrum's edges:

$$\Gamma_{\mathrm{BBS}}(u) = \int_{\omega_l}^{\omega_h} S(\omega)e^{j\omega u}d\omega = \frac{1}{ju}\left[S(\omega_h)e^{j\omega_h u} - S(\omega_l)e^{j\omega_l u}\right] + O(u^{-2}) \tag{9}$$

Since the steeper edge in the spectrum of Fig. 6(a) is located at the longer wavelength, then $S(\omega_l) \gg S(\omega_h)$ and the second term in brackets dominates over the first. The asymptotic phase depicted in Fig. 6(c), once referred to the central frequency, evolves with a negative slope $\omega_l - \overline{\omega}$.

Optics EXPRESS

In a further set of experiments we explored the system's ability to perform FT spectroscopy. The raw spectral resolution is $\delta\nu = 1.21/(2u_{\max}) = 11$ GHz (90 pm), which is lower by a factor of two with respect to previous demonstrations based on conventional amplitude modulation and the same RF bandwidth [37]. This value increases up to 14 GHz after windowing the interferogram with our default $\beta = 3$ Kaiser-Bessel window, introduced to reduce the ripples around sharp spectral features.

We first analyzed, using scheme B in Fig. 1, a commercial FBG WDM array (FBGS) built in low bend loss fiber and composed of five weak uniform FBG with length 4 mm, FWHM of 0.18 nm, and reflectivities in the range 7.4% to 8.7%, starting at a wavelength of ~1546 nm, increasing in nominal steps of 2 nm, and mutually separated by 1 m. The amplitude and phase of the complex interferogram is depicted in Fig. 7(a), and its FT spectrum plotted in blue in Fig. 7(b). In this last plot we also show with an orange trace its OSA spectrum. The interferogram is thus the amplitude and phase of five oscillations with approximately equal power and frequency spacing. When these frequencies are in phase, the interferogram's amplitude shows clear peaks that allow for the observation of an envelope of triangular shape, extending up to the nominal length of the individual FBG. This triangular shape reflects the fact that, being weak, the FBG's amplitude reflection coefficient $r(\omega)$ follows a sinc function, and so its reflectivity $R(\omega) = |r(\omega)|^2$ is a sinc^2. In the central peaks of Fig. 7(a), the phase returns to the initial zero value after periodic excursions, but the pattern is progressively lost due to the imbalance of reflected power and frequency spacing between reflectors. This experiment also permits the estimation of the displayed noise floor: the BBS used for illumination had an approximately flat spectral density of +14 dBm in 20 nm and so, and taking into account the FBG reflectivity, the noise floor of Fig. 7(b) is about −35 dBm/nm.

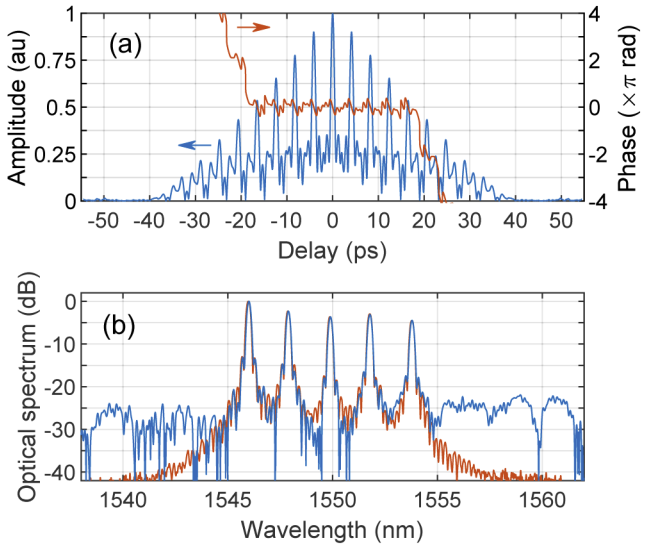

Fig. 7. (a) Amplitude and phase of the complex interferogram $\Gamma(u)$ of the WDM FBG array. A linear phase term accounting for the array's spectral center has been added to help its visualization. (b) FT (blue) and OSA (orange) traces of the spectrum reflected in the WDM FBG array. The differences in the spectral peaks are mostly due to the non-uniform spectral density of the BBS used for illumination.

We then performed some additional characterizations of our FT spectra. In Fig. 8(a) we show the spectra of monochromatic lines at 1540, 1545, 1555 and 1560 nm extracted from our TLS and directed to the first modulator with a power of 2 dBm. Here, the complex interferograms

Optics EXPRESS

were windowed with a Kaiser-Bessel window with $\beta = 6$ (spectral resolution of 19 GHz) to display the full dynamic range. The line at the normalization wavelength of 1550 nm represents the window used. In these measurements we observe a dynamic range of ~23 dB and extracted a maximum variation in power of 0.6 dB, mostly due to the non-uniform insertion loss of our CFBG. We also found a wavelength deviation with respect to the nominal TLS value <40 pm in all cases, of the same order of our previous analysis of the normalization trace in Fig. 4.

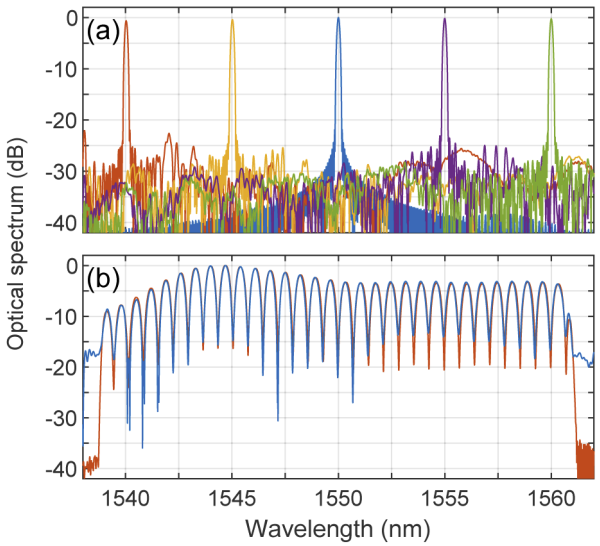

Fig. 8. (a) FT spectrum of laser lines at 1540, 1545, 1555, and 1560 nm. The line at 1550 nm represents the window used. (b) FT (blue) and OSA (orange) traces of the BBS spectrum reflected in a microscope slide.

Second, we compared in Fig. 8(b) the reflected spectra of a 1.1-mm thick microscope slide, illuminated by our BBS and placed again in position B of Fig. 1, with an OSA measurement. The OSA trace, taken from the detector's side, undergoes the same non-uniform CFBG loss as the FT spectrum, and therefore allows for a comparison of the relative precision in wavelength and power by comparing the multiple peaks. We found rms deviations of 0.3 dB in power and 30 pm in wavelength, slightly lower than our estimates due to environmental changes.

In a final example we performed an OLCR experiment targeted to the analysis of a commercial 1-mm long apodized uniform FBG written in SMF (Technica T10, peak wavelength 1550.20 nm, FWHM 1.6 nm, reflectivity 51%). The BBS was used to feed a composite fiber/free space interferometer whose arms are built from a dielectric mirror and the FBG, placed in the position of the DUT in scheme C of Fig. 1. The interferometer's output field $\mathcal{E}_T(t)$ is the sum of the BBS field reflected from the mirror, $\mathcal{E}_{BBS}(t)$, and from the FBG, $\mathcal{E}_{FBG}(t)$, so that the autocorrelation $\Gamma_T(u) = \langle \mathcal{E}_T(t)^* \mathcal{E}_T(t+u) \rangle$ is given by:

$$\Gamma_T(u) = \Gamma_{BBS}(u) + \Gamma_{FBG}(u) + \langle \mathcal{E}_{BBS}(t)^* \mathcal{E}_{FBG}(t - t_0 + u) \rangle + \langle \mathcal{E}_{FBG}(t - t_0)^* \mathcal{E}_{BBS}(t+u) \rangle \quad (10)$$

with $\Gamma_{BBS}(u)$ and $\Gamma_{FBG}(u)$ the corresponding autocorrelations of BBS and FBG. In Eq. (10) we have introduced a delay t_0 to account for a displacement from the equal-path position in order to isolate the cross-correlation terms between BBS and FBG. The Fourier transform of the first of these terms is $S(\omega) r(\omega) e^{-j\omega t_0}$, with $r(\omega)$ the FBG's amplitude reflection coefficient. Since $S(\omega)$ is constant in the FBG's reflection band, the cross-correlation is proportional to the FBG's impulse response $h(u)$, which is the IFT of $r(\omega)$, shifted in time by t_0. The relevant resolution is

Optics EXPRESS

thus the one-point temporal resolution δu, as it represents the temporal step upon which function $h(u)$ is retrieved.

The results are presented in Fig. 9. In Fig. 9(a) we depict both the FT and OSA spectra and in Fig. 9(b), with a blue trace, the inteferogram's amplitude as a function of distance in fiber, $z = cu/(2n_g)$. The autocorrelation terms of this last trace were subtracted by performing two additional measurements, each with one of the interferometer's arms blocked. After this subtraction, the cross-correlation amplitude is isolated as shown by the orange trace. The sub-micron resolution permits the observation of the standard structure of the apodized FBG's impulse response [43–45], namely a main smooth peak due to the strong reflection of wavelengths close to the Bragg wavelength, followed by a secondary peak due to the more internal reflections of wavelengths far from the Bragg condition. Finally, we recall that the cross-correlation $\langle \mathcal{E}_{\mathrm{BBS}}(t)^* \mathcal{E}_{\mathrm{FBG}}(t - t_0 + u) \rangle$ is proportional to the phase term describing the OPD difference between interferometer's arms, so that the cross-correlation amplitude, in contrast to the phase, does not depend on the interferometer's stability [26]. In our case, unfortunately, our external interferometer used to place the DUT was not sufficiently stable to provide a complete, vector characterization of the FBG in the time domain.

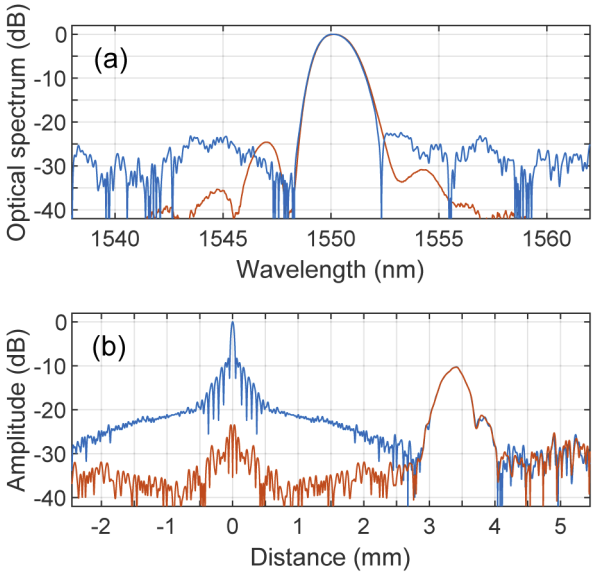

Fig. 9. (a) Reflected optical spectrum in the 1-mm, apodized FBG: blue, FT spectrum; orange, OSA spectrum. (b) Blue: amplitude of the low-coherence interferogram. Orange: cross-correlation term. The trace's resolution $\delta z = c\delta u/(2n_g)$ is 550 nm in fiber.

5. Conclusions

We have presented a simple and versatile phase sensitive LCI system built on MWP concepts, with C-band applications in spectral analysis and reflectometric characterization of components. The control of the interferogram's phase is attained by a direct normalization of the MW amplitude and phase transfer in a dispersive MWP link based on electro-optic modulation and down-conversion. This architecture can be simplified further by operating a single modulator bidirectionally [46–48], so that the tasks of modulation and down-conversion are performed by the same device, or by using a frequency chirp instead of the sequential delivery of frequencies used here. The LCI system provides high resolution scans (5.45 fs in the time domain or 1.63 μm in free space) of a total temporal range of 54.5 ps, or 16.3 mm of OPD, range that can be

Optics EXPRESS

increased by both dispersion and RF bandwidth. For OLCR experiments in fiber, the obtained one-point resolution is 0.55 μm in a range of 5.5 mm.

With respect to the spectral analysis, the present MWP LCI system shows a 14-GHz spectral resolution after windowing, a figure which is close to commercial FT spectrometers or grating-based dispersive OSA and can be increased by extending the temporal range $u_{\max}$. The wavelength range, however, is limited by the CFBG's reflection band. This shortcoming can be partially overcome by use of DDL based on dispersive fiber, since in that case the wavelength range could be extended to the operation range of the electro-optic modulators. This would require, however, HOD compensation and the monitoring of the dispersive delays used for the OPD scan. The moderate value of the obtained dynamic range (~23 dB) also deserves further study and, in particular, the limitations imposed by the CFBG's phase ripple, which have not been addressed in the present investigation. The noise floor is expected to decrease by use of electro-optical heterodyne down-conversion [49], as similar approaches have demonstrated sensitivity values down to −90 dB in incoherent optical frequency-domain reflectometers (OFDR) [50]. Similar considerations apply to the comparison with conventional LCI and OLCR instruments, which outperform the values of OPD range and sensitivity presented here at the expense of overall system's complexity.

In comparison with OFDR instruments devoted to the optical vector analysis of C-band components, systems which are based on the wavelength scan of a tunable laser at ~pm steps [51], the present demonstration cannot compete in terms of spectral resolution, and also shows the limitation of dynamic range and sensitivity mentioned above. As a reflectometer, OFDR offers resolutions that can be as low as 5 μm [52,53] in ranges of tens of meters [51], ranges that are typically beyond the reach of low-coherence reflectometers. In this regard, the main advantage of the present approach, in addition to its simplicity, is its high spatial or temporal resolution. The analysis of interferograms with fs resolution and the sub-μm characterization of components represent examples of this advantage. The proposed LCI approach, in summary, constitutes a potentially compact and versatile technique for the high-resolution characterization of components and devices using MWP.

Funding

Agencia Estatal de Investigación (TEC2017-89688-P); Conselleria de Cultura, Educación y Ciencia, Generalitat Valenciana (ACIF/2016/214).

Disclosures

The authors declare no conflicts of interest.

References

1. D. Derickson, *Fiber optics test and measurement* (Prentice Hall, 1998).
2. A. D. Kersey, A. Dandridge, A. B. Teveten, and T. G. Giallorenzi, "Single-mode fibre Fourier transform spectrometer," Electron. Lett. **21**(11), 463–464 (1985).
3. K. Takada, M. Kobayashi, and J. Noda, "Fiber optic Fourier transform spectrometer with a coherent interferogram averaging scheme," Appl. Opt. **29**(34), 5170–5176 (1990).
4. M. A. Davis and A. D. Kersey, "Application of a fiber Fourier transform spectrometer to the detection of wavelength encoded signals from Bragg grating sensors," J. Lightwave Technol. **13**(7), 1289–1295 (1995).
5. P. Beaud, J. Schutz, W. Hodel, H. P. Weber, H. H. Gilgen, and R. P. Salathé, "Optical reflectometry with micrometer resolution for the investigation of integrated optical devices," IEEE J. Quantum Electron. **25**(4), 755–759 (1989).
6. P. Lambelet, P. Y. Fonjallaz, H. G. Limberger, R. P. Salathé, C. Zimmer, and H. H. Gilgen, "Bragg grating characterization by optical low-coherence reflectometry," IEEE Photonics Technol. Lett. **5**(5), 565–567 (1993).
7. M. Volanthen, H. Geiger, M. J. Cole, R. I. Laming, and J. P. Dakin, "Low coherence technique to characterise reflectivity and time delay as a function of wavelength within a long fibre grating," Electron. Lett. **32**(8), 757–758 (1996).
8. S. D. Dyer, K. B. Rochford, and A. H. Rose, "Fast and accurate low-coherence interferometric measurements of fiber Bragg grating dispersion and reflectance," Opt. Express **5**(11), 262–266 (1999).

Optics EXPRESS

9. P. Giaccari, H. G Limberger, and R. P. Salathé, "Local coupling-coefficient characterization in fiber Bragg gratings," Opt. Lett. **28**(8), 598–600 (2003).
10. A. F. Fercher, W. Drexler, C. K. Hitzenberger, and T. Lasser, "Optical coherence tomography-principles and applications," Rep. Prog. Phys. **66**(2), 239–303 (2003).
11. D. Stifter, "Beyond biomedicine: a review of alternative applications and developments for optical coherence tomography," Appl. Phys. B **88**(3), 337–357 (2007).
12. A. Koch and R. Ulrich, "Fiber-optic displacement sensor with 0.02 μm resolution by white-light interferometry," Sensor. Actuat. A-Phys. **25**(1-3), 201–207 (1990).
13. A.-F. Obaton, C. Palavicini, Y. Jaouën, E. Kerrinckx, Y. Quiquempois, and M. Lièvre, "Characterization of fiber Bragg gratings by phase-sensitive optical low-coherence reflectometry," IEEE Trans. Instrum. Meas. **55**(5), 1696–1703 (2006).
14. R. Gabet, P. Hamel, Y. Jaouën, A.-F. Obaton, V. Lanticq, and G. Debarge, "Versatile characterization of specialty fibers using the phase-sensitive optical low-coherence reflectometry technique," J. Lightwave Technol. **27**(15), 3021–3033 (2009).
15. V. Gaillard, X. Aduriz, N. Daher, X. Chapeleau, D. Leduc, C. Lupi, N. Traynor, P. Casari, and C. Boisrobert, "Local and spectral characterization of optical fibers and fiber Bragg gratings with low coherence interferometry," Fiber Integrated Opt. **28**(1), 108–126 (2009).
16. J. Hervás, A. L. Ricchiuti, W. Li, N. H. Zhu, C. R. Fernández-Pousa, S. Sales, M. Li, and J. Capmany, "Microwave photonics for optical sensors," IEEE J. Sel. Top. Quantum Electron. **23**(2), 327–339 (2017).
17. L. R. Chen, M.-I. Comanici, P. Moslemi, J. Hu, and P. Kung, "A review of recent results on simultaneous interrogation of multiple fiber Bragg grating-based sensors using microwave photonics," Appl. Sci. **9**(2), 298 (2019).
18. J. Mora, B. Ortega, A. Díez, J. L. Cruz, M. V. Andrés, J. Capmany, and D. Pastor, "Photonic microwave tunable single-bandpass filter based on a Mach-Zehnder interferometer," J. Lightwave Technol. **24**(7), 2500–2509 (2006).
19. M.-I. Comanici, L. R. Chen, and P. Kung, "Interrogating fiber Bragg grating sensors based on single bandpass microwave photonic filtering," in *Proceedings of the 2010 IEEE International Topical Meeting on Microwave Photonics* (IEEE, 2010), pp. 377–380.
20. H. Chen, S. Zhang, H. Fu, B. Zhou, and N. Chen, "Sensing interrogation technique for fiber-optic interferometer type of sensors based on a single-passband RF filter," Opt. Express **24**(3), 2765–2773 (2016).
21. J. Benítez, M. Bolea, and J. Mora, "Demonstration of multiplexed sensor system combining low coherence interferometry and microwave photonics," Opt. Express **25**(11), 12182–12187 (2017).
22. S. Zhang, R. Wu, H. Chen, H. Fu, J. Li, L. Zhang, M. Zhao, and D. Zhang, "Fiber-optic sensing interrogation system for simultaneous measurement of temperature and transversal loading based on a single-passband RF filter," IEEE Sensors J. **17**(7), 2036–2041 (2017).
23. C. R. Fernández-Pousa, H. Maestre, and P. Corral, "Interferometric displacement sensor by use of a single-passband incoherent microwave photonics filter," Proc. SPIE **9157**, 9157AD (2014).
24. Y. Deng, M. Li, N. Huang, H. Wang, and N. Zhu, "Optical length-change measurement based on an incoherent single-bandpass microwave photonic filter with high resolution," Photonics Res. **2**(4), B35–B39 (2014).
25. J. Benítez and J. Mora, "Low-coherence interferometry using microwave photonics for multilayered samples," J. Lightwave Technol. **36**(19), 4611–4617 (2018).
26. C. R. Fernández-Pousa, J. Mora, H. Maestre, and P. Corral, "Radio-frequency low-coherence interferometry," Opt. Lett. **39**(12), 3634–3637 (2014).
27. Y.-J. Rao and D. A. Jackson, "Recent progress in fibre optic low-coherence interferometry," Meas. Sci. Technol. **7**(7), 981–999 (1996).
28. J. Benítez, M. Bolea, and J. Mora, "High-performance low coherence interferometry using SSB modulation," IEEE Photonics Technol. Lett. **29**(1), 90–93 (2017).
29. J. Benítez, M. Bolea, and J. Mora, "Advanced RF interferometry structure for improving operation range," IEEE Photonics Technol. Lett. **30**(18), 1637–1640 (2018).
30. L. Li, X. Yi, S. X. Chew, S. Song, L. Nguyen, and R. A. Minasian, "Double-pass microwave photonic sensing system based on low-coherence interferometry," Opt. Lett. **44**(7), 1662–1665 (2019).
31. J. Benítez, M. Bolea, and J. Mora, "SCM adaptation to improve scanning rate in RF interferometry applications," IEEE Photonics Technol. Lett. **29**(12), 999–1002 (2017).
32. J. Benítez, M. Bolea, and J. Mora, "Sensitivity enhancement for low-coherence interferometry," IEEE Photonics Technol. Lett. **29**(20), 1735–1738 (2017).
33. B. Qi, A. Tausz, L. Qian, and H.-K. Lo, "High-resolution, large dynamic range fiber length measurement based on a frequency-shifted asymmetric Sagnac interferometer," Opt. Lett. **30**(24), 3287–3289 (2005).
34. B. Qi, L. Qian, A. Tausz, and H.-K. Lo, "Frequency-shifted Mach-Zehnder interferometer for locating multiple weak reflections along a fiber link," IEEE Photonics Technol. Lett. **18**(1), 295–297 (2006).
35. F. Ye, Y. Zhang, B. Qi, and L. Qian, "Frequency-shifted interferometry – a versatile fiber-optic sensing technique," Sensors **14**(6), 10977–11000 (2014).
36. G. Peraita, A. J. Torregrosa, H. Maestre, and C. R. Fernández-Pousa, "Broadband linearization of dispersive delay line using a chirped fiber Bragg grating," IEEE Photonics Technol. Lett. **27**(10), 1044–1047 (2015).
37. J. Clement Bellido and C. R. Fernández-Pousa, "Spectral analysis using a dispersive microwave photonics link based on a broadband chirped fiber Bragg grating," J. Lightwave Technol. **33**(20), 4207–4214 (2015).

Optics EXPRESS

38. O. Lopez, A. Amy-Klein, C. Daussy, C. Chardonnet, F. Narbonneau, M. Lours, and G. Santarelli, "86-km optical link with a resolution of 2×10^{-18} for RF frequency transfer," Eur. Phys. J. D **48**(1), 35–41 (2008).
39. X. Yi, T. X. H. Huang, L. Li, and R. A. Minasian, "Overcoming tap-delay-variation induced distortion in microwave photonic filters," IEEE Photonics Technol. Lett. **24**(8), 691–693 (2012).
40. A. Kohlhaas, C. Fromchen, and E. Brinkmeyer, "High-resolution OCDR for testing integrated-optical waveguides: Dispersion-corrupted experimental data corrected by a numerical algorithm," J. Lightwave Technol. **9**(11), 1493–1502 (1991).
41. A. F. Fercher, C. K. Hitzenberger, M. Sticker, R. Zawadzki, B. Karamata, and T. Lasser, "Numerical dispersion compensation for partial coherence interferometry and optical coherence tomography," Opt. Express **9**(12), 610–615 (2001).
42. C. M. Bender and S. A Orszag, *Asymptotic Methods and Perturbation Theory* (Springer, 1999), Chap. 6.
43. G. A. Cranch and G. M. H. Flockhart, "Tools for synthesising and characterising Bragg grating structures in optical fibres and waveguides," J. Mod. Opt. **59**(6), 493–526 (2012).
44. A. Carballar and M. A. Muriel, "Phase reconstruction from reflectivity in fiber Bragg gratings," J. Lightwave Technol. **15**(8), 1314–1322 (1997).
45. J. Azaña and M. A. Muriel, "Study of optical pulses-fiber gratings interaction by means of joint time-frequency signal representations," J. Lightwave Technol. **21**(11), 2931–2941 (2003).
46. J. Clement, H. Maestre, G. Torregrosa, and C. R. Fernández-Pousa, "Incoherent optical frequency domain reflectometry using balanced frequency-shifted interferometry in a downconverted phase-modulated link," in *Proceedings of the 2018 IEEE International Topical Meeting on Microwave Photonics* (IEEE, 2018), pp. 1–4.
47. S. Werzinger, L.-S. Härteis, M. Koeppel, and B. Schmauss, "Time and wavelength division multiplexing of fiber Bragg gratings with bidirectional electro-optical frequency conversion," in *26th International Conference on Optical Fiber Sensors, OSA Technical Digest* (Optical Society of America, 2018), paper ThE19.
48. H. Guo, A. Gnanapandithan, Y. Liu, C. Zhou, Z. Zheng, Y. Ou, X. Zeng, and L. Qian, "Single-arm frequency-shifted interferometry using a bidirectional electro-optic modulator," J. Lightwave Technol. **37**(4), 1310–1316 (2019).
49. D. W. Dolfi and M. Nazarathy, "Optical frequency domain reflectometry with high sensitivity and resolution using optical synchronous detection with coded modulators," Electron. Lett. **25**(2), 160–162 (1989).
50. J. Clement, H. Maestre, G. Torregrosa, and C. R. Fernández-Pousa, "Incoherent optical frequency-domain reflectometry based on homodyne electro-optic downconversion for fiber-optic sensor interrogation," Sensors **19**(9), 2075 (2019).
51. B. J. Soller, D. K. Gifford, M. S. Wolfe, and M. E. Froggatt, "High resolution optical frequency domain reflectometry for characterization of components and assemblies," Opt. Express **13**(2), 666–674 (2005).
52. K. Iizuka and S. Fujii, "A fault locator for integrated optics," in *Optical Fiber Sensors, Collected Papers of the International Conferences on Optical Fiber Sensors 1983-1997* (Optical Society of America, 1992), paper Th32.
53. D. Zhao, D. Pustakhod, K. Williams, and X. Leijtens, "High resolution optical frequency domain reflectometry for analyzing intra-chip reflections," IEEE Photonics Technol. Lett. **29**(16), 1379–1382 (2017).